Interferometric characterization of growth dynamics during dendritic electrodeposition of zinc

F. Argoul,[1] E. Freysz,[2] A. Kuhn,[1,*] C. Léger,[1] and L. Potin[1]
[1]*Centre de Recherche Paul Pascal, Avenue Schweitzer, 33600 Pessac, France*
[2]*Centre de Physique Moléculaire Optique et Hertzienne, 351 Cours de la Libération, 33405 Talence, France*
(Received 28 July 1995)

We propose a dynamical interferometric analysis of the electrodeposition of zinc in thin gap cells without supporting electrolyte. The emphasis is made on the dendritic regime, which is observed under high current conditions. We show that the growth process can be split into four different stages: a fast polarization of the interface, a two-step depletion regime where the metallic interface encounters two successive destabilizations, and a large field screening regime leading to few dendrites.

PACS number(s): 68.45.−v, 07.60.Ly, 47.54.+r, 68.35.Fx

I. INTRODUCTION

Electrodeposition in thin gap geometry has proved in the past ten years [1–4] to be a very attractive experiment for the application of theories on fractal growth processes and the confrontation with numerical models such as diffusion-limited aggregation (DLA). But this rapid success was in some sense harmful, since investigations of the detailed physicochemical processes which can arise in thin gap geometry electrochemical cells were screened by the attraction of the scientific community for fractals. Only very recently several experimental investigations [5–12] of the chemistry and the physics of electrodeposition processes in quasi-two-dimensional cells have been performed. They showed that, not only competitive chemical reactions such as proton, oxygen, and alkali-metal cation reduction [8,9] can modify both the structure and the composition of the deposit, but also additional transport processes such as buoyancy driven convection [10] and electroconvection [7] can play a major role, besides diffusion and migration, for the renewing of the growing interface in electroactive species.

Different methods, such as ethylenediamine tetraacetic acid (EDTA) titrations [10,11], Normasky phase contrast [7], the schlieren method [13,14], and interferometric techniques [15–17] have been independently used to evidence the concentration profiles which are likely to appear in thin gap electrodeposition experiments. Nevertheless, very few of them provided improvements in the knowledge of the dynamics of zinc electrodeposition in correlation with the transport processes. Interferometry has proved to be a very efficient way for getting information about the different transport processes that can arise in electrochemical cells. Many experimental and theoretical studies have been performed since the early 1970's to analyze buoyancy driven convection in thick electrochemical cells (gap ~10 mm) [18–22]. Unfortunately these analyses were limited to the characterization of steady state concentration profiles in the neighborhood of the cathode and the anode. Very few discussions of the morphology dependence on the transport were attempted. In a more recent work, Barkey *et al.* [15] have used a Mach-Zehnder interferometer to measure concentration profiles in thin electrochemical cells. Although their discussion on transport processes was confirmed by quantitative measurements of the local velocity [10], their interest was rather on the morphology than on the dynamics of the growth process.

In this paper, we show that important information about the dynamics of the growth can be extracted from interferometric determination of the concentration profiles. Interferometry [18] is well adapted in this respect since it is a nonintrusive method. We take advantage of this technique to enlighten the mechanisms that influence the different stages of the growth. We show that the dendritic growth regime which takes place under high concentration and high current conditions is indeed a complex succession of distinct regimes: a first interfacial polarization regime, a two-step depletion regime where a nonstationary convective diffusion mechanism settles and during which the interface encounters two successive destabilizations, and finally a last regime which is peculiar to high current conditions where only a few dendrites emerge from the convective diffusion roll and strongly screen all their neighbors.

The experimental setup and the basic principles of the interferometric analysis are presented in Sec. II of this paper. In Sec. III, we propose a global picture of the dynamics of dendritic growth in the electrodeposition of zinc, based on the confrontation of macroscale interferometric patterns and voltage signal recording. In Sec. IV, we focus the interferometer on smaller scales and we evidence a narrow band of strong gradients in the close neighborhood of the active part of the interface. Finally, in Sec. V, we concentrate on the late stage of the growth.

II. EXPERIMENTAL APPARATUS

To measure the concentration field around the zinc electrodeposit, in thin gap geometry, we have built a

*Present address: California Institute of Technology, Division of Chemistry and Chemical Engineering, Pasadena, CA 91125.

 ©1996 The American Physical Society

Mach-Zehnder interferometer [23,24]. The experimental setup is presented in Fig. 1. The output of a 10 mW TEM_{00} He-Ne laser is spatially filtered and split by means of a half-wave (QW1) and polarizing cube (PC) beam splitter into the two arms of the interferometer. While QW1 adjusts the intensity balance in the two arms of the interferometer, a second half-wave plate (QW2) equalizes the polarization of the two beams at the exit of the interferometer where a 50% beam splitter (BS1) is introduced. To compensate any length mismatch between the two arms of the interferometer, the mirror M1 of the Mach-Zehnder interferometer is mounted on a piezoelectric crystal (PZT). The equilibrium position of the Mach-Zehnder is obtained when the two beams before BS1 are of equal intensity. Deviations from this equilibrium position can be balanced with an electronic feedback loop acting on the piezoelectric crystal. The error signal used to adjust dynamically the interferometer is based on the difference of the intensity received by the two photodiodes PD1 and PD2. Before the electrodeposition experiment starts, less than one fringe is observed in the shined zone (infinite fringe spacing [18]). At the exit of the interferometer, two different magnification images of the electrodeposition cell can be made on two charged couple device (CCD) cameras, coupled to a video screen and a computer equipped with a frame grabber and an image analyzer. To avoid the observation of coherent optical artifacts on the image of the aggregates, the electrodeposition cell can also be observed with an incoherent light source. With this setup, both small (10 μm) and large scale (1 cm) observations of the cell can be made. The cells for the electrodeposition are made of two closely spaced glass optical étalon slides ($\lambda/4$ over 50×50 mm flatness) sandwiching a layer of $ZnSO_4$ aqueous solution. Two straight parallel zinc wires (cathode and anode with purity 99.99% and diameter 250 μm), are tightly confined between the two glass slides and also play the role of spacers. The schematic of this electrochemical cell has been given in a previous publication [10]. The electrolyte was prepared from deionized water and 99.9% purity $ZnSO_4$ cleaned of any trace of dissolved oxygen by bubbling nitrogen through it for 1 hour. The experiments were performed at fixed current intensity and at room temperature ($\sim$20°C). The voltage drop between cathode and anode has also been recorded with a high frequency 16 bit analog-to-digital converter (ADC) coupled to a microcomputer.

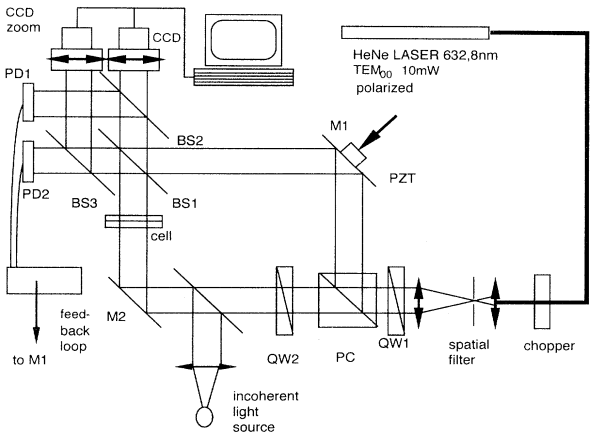

FIG. 1. Experimental setup: optoelectronic assisted Mach-Zehnder interferometer. (QW1 and QW2 symbolize half-wave plates.)

The experimental setup is basically suited for measuring refractive index modifications inside the electrolytic cell. The variation of light intensity produced by the interference of the two beams takes the generic form [23,24]

$$I(x,y)=I_0\{1+m\cos[2\pi\delta(x,y)/\lambda]\}\ , \tag{1}$$

where I_0 is the background intensity, λ the wavelength of the laser (632.8 nm), m the modulation (contrast) of fringes, and $\delta(x,y)$ the spatial variation of the length between the two arms of the interferometer. This intensity is both sensitive on focus errors, alignment errors, and optical aberration errors that lead to a decrease of the signal to noise ratio (SNR). Therefore a fundamental prerequisite for obtaining contrasted fringe pattern is to ensure the homogeneity of the light intensity before applying the current. Any fluctuation of light will affect the local phase of the interfering waves and will delocalize the fringes. As a consequence, high quality optics and high quality glass plates for the electrochemical cell ($\lambda/4$ flatness over 50×50 mm) are required. The maximum SNR is obtained when the contrast of fringes m is maximum. This is practically realized by adjusting the intensity and the polarization of the two beams. To further improve the homogeneity of the light and of the image, we have minimized the aperture of the laser beam and corrected the astigmatism introduced by the beam splitter. The feedback loop through the piezoelectric crystal is also crucial for maintaining a stable phase reference in the bulk and measuring accurately the dynamical evolution of the concentration field close to the interface. Presently, we can reach a maximum 90% uniformity over a surface of 4 cm^2. This limitation is due to the diffraction by the edges of the optics, stripes, and unavoidable residual dust. These limitations will be overcome in the future with a holographic technique. Provided these artifacts have been minimized, one can assume a linear approximation of the spatial phase variation

$$\delta(x,y)=dn(x,y)\ , \tag{2}$$

where $d=250\ \mu\text{m}\pm5\ \mu\text{m}$ is the thickness of the solution confined between two glass plates and $n(x,y)$ is the spatial refractive index of the solution. The dependence of the refractive index $n(x,y)$ of a zinc sulfate solution versus its concentration $C(x,y)$ is usually given for sodium light sources and we had therefore to perform the calibration for a He-Ne laser source with a refractometer (at 20°C) before exploiting our fringe patterns:

$$n(x,y)=1.3313+0.0232C(x,y)\ . \tag{3}$$

The combination of Eqs. (1) and (3) gives an approximate relation for the difference of concentration between two subsequent fringes as a function of the depth d of the cell:

$$\Delta(C) \simeq \frac{\lambda}{0.0232d} \ . \tag{4}$$

In particular, with 250 μm depth cells, the concentration difference between two fringes will be about 0.11 mol l^{-1}. Therefore, the lowest concentration of zinc sulfate solution that can be used with this gap is about 0.1 mol l^{-1}, since a minimum of one fringe is necessary to compute the concentration by interpolation. Typically, in front of the electrodeposit, one can therefore expect to observe five fringes for an initial 0.5 mol l^{-1} solution.

III. MACROSCOPIC INTERFEROMETRIC ANALYSIS

In this section we focus on the large scale analysis of the dynamics of zinc electrodeposition in thin gap geometry.

A. Interferometric patterns

It has been shown recently in zinc electrodeposition that, if oxygen is carefully extracted by nitrogen bubbling, the principal type of morphology that can be observed in high current galvanostatic experiments is dendritic [8,11]. These dendrites can be more or less branched, depending on the strength of the electric field. We show in Fig. 2 the result of the interferometric analysis for two different current intensities. In the top picture of Fig. 2 (low field regime) the growth pattern presents many sidebranches reflecting the underlying hexagonal symmetry of the zinc crystal. In the bottom image of Fig. 2 (high field regime) one single sharp whisker is leading the growth and captures the whole current density on its tip; strong electric screening of the neighboring branches is evidenced. The great advantage of the interferometric analysis comes from the fact that even on static images like those presented in Fig. 2, the way the fringes are distributed around the metallic aggregate gives information on the dynamics of the growth process and helps in predicting the future evolution of the growth. We observe that these fringes, which are nothing but isoconcentration lines, bring us a visualization of the way the selection between branches proceeds in these two different cases. Let us note that in the top picture of Fig. 2 the spacing of the isoconcentration fringes ahead of the leading tips is very similar from one branch to the next one, while on the bottom picture, the fringes ahead of the leading spike are much more closely packed in space than those of other branches, proving that this taller spike is leading the growth by its greater velocity (steeper concentration gradient). There is in fact an intricate interplay between the morphology and the dynamics of the growth because the metal interface is moving and the concentration profile is constantly evolving accordingly.

B. Fringe patterns analysis

We show in Fig. 3 five successive snapshots of interferometric patterns on both cathodic and anodic sides, recorded in two experimental runs. From Fig. 3(a) to Fig. 3(c), we observe the emergence and the propagation of equally spaced fringes (equiconcentration lines) from the cathode and from the anode. During these first 240 s, the interface of the cathode does not seem to change much at the scale of our observation and the fringe pattern is quite symmetric on cathodic and anodic sides. From Fig. 3(c) to Fig. 3(e) a multitude of sharp dendrites emerge from the cathode and progressively distorts the initially flat fringes. The growth is unstable on the cathode because as soon as one dendrite overtakes the other ones, it keeps and amplifies its advantage and screens its neighbors. On the anode, the fringes are piling up because the oxidation of the zinc metal is constantly feeding the anode interface with metal cations. We can already, from this large scale analysis, distinguish two different stages of the growth.

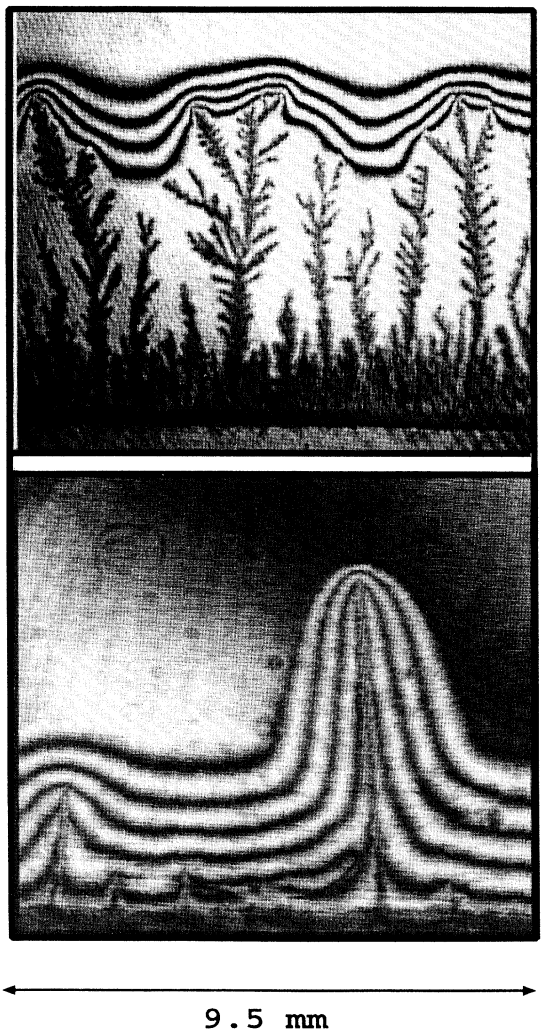

FIG. 2. Grey scale representation of interferometric imaging of the concentration field around zinc electrodeposits. The experimental parameters are, respectively, (a) [$ZnSO_4$] = 1 mol l^{-1}, j=50 mA cm^{-2}, (b) [$ZnSO_4$] = 0.5 mol l^{-1}, j=150 mA cm^{-2}. The geometrical characteristics of the cell are width W=5 cm, length L=5 cm, depth D=125 μm in (a) and D=250 μm in (b).

(i) A first phase of "cathodic depletion" where the concentration in the neighborhood of the cathode is progressively decreasing and a finite set of fringes invades this part of the cell [panels (a) to (c)].

(ii) A second phase where the interfacial concentration approaches zero, the cathode becomes unstable, and a selection mechanism takes place inside the concentration gradient region [panels (d) and (e)].

Assuming that Eqs. (1) and (3) are valid for the light intensity dependence on the concentration, we can reconstruct, from successive interferograms selected in this depletion regime (before the dendrites emerge from the cathode), the concentration profiles given in Fig. 4(a). Both anodic and cathodic sites are represented and we notice in these plots a slight difference between the shapes of these curves which was imperceptible on the pictures of Fig. 3. On the cathodic side of the cell, the

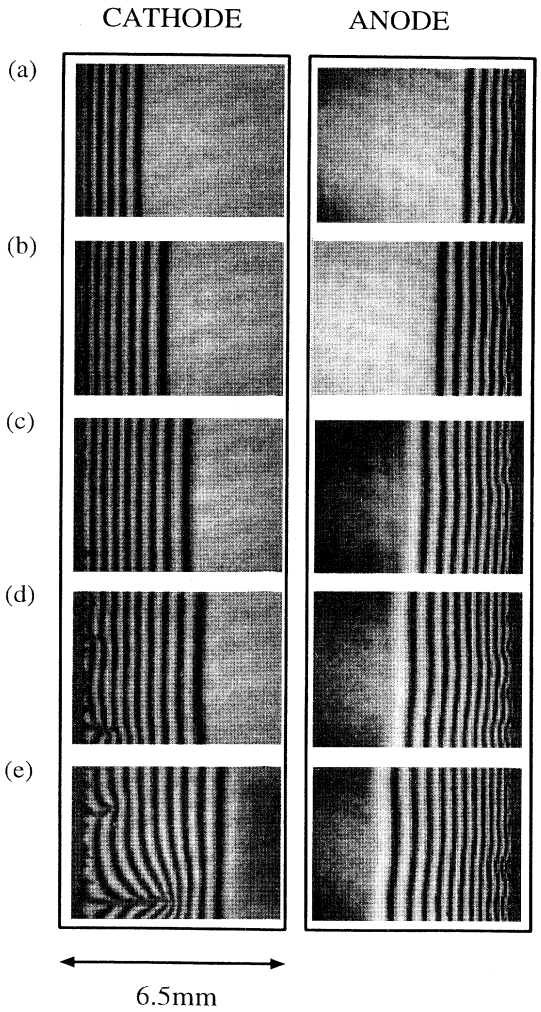

FIG. 3. Macroscopic interferometric images of thin gap electrodeposition of zinc at different times of the growth process. (a), (b), (c), (d), and (e) are digitized pictures given by the Mach-Zehnder at five successive times $t=85$ s, $t=150$ s, $t=240$ s, $t=300$ s, $t=440$ s, respectively. The parameter values are $[ZnSO_4] = 1$ mol l^{-1}, $j=150$ mA cm^{-2}, $W=5$ cm, $L=5$ cm, and $D=250$ μm.

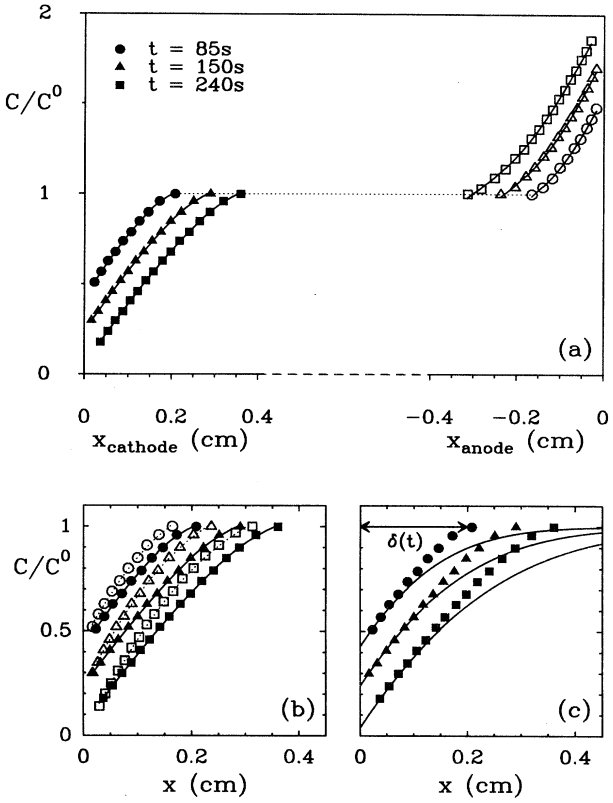

FIG. 4. (a) Large scale concentration profiles computed from the interferometric pattern in the first stage of the growth. (b) Comparison of the anodic and cathodic profiles of (a). (c) The three concentration profiles are compared with the theoretical profiles computed from the diffusion equation solution (5). Error bars have been omitted for the sake of clarity of the picture. Let us mention that the uncertainty on the x position is less than 0.10 cm. The parameter values are $[ZnSO_4] = 1$ mol l^{-1}, $j=150$ mA cm^{-2}, $W=5$ cm, $L=5$ cm, and $D=250$ μm.

concentration profiles are very similar to those which can be encountered in convective diffusion systems (Nernst diffusion layer). This aspect will be discussed in the next paragraph. On the anodic side, the concentration profiles proceed more slowly towards the cathode and present a greater curvature than on the cathodic side. This difference is more visible when one superimposes both plots, as done in Fig. 4(b). This bending of the anodic profiles is the consequence of the increase of the viscosity as one gets closer to the anode.

As mentioned above, these concentration profiles are definitely different from those observable in purely diffusion limited systems. Let us recall the general solution of the one-dimensional diffusion equation $\partial C/\partial t = D\partial^2 C/\partial x^2$ with fixed flux boundary conditions (constant current density):

$$C(x,t)=C^0-\frac{j}{nFD_0}\left\{2\sqrt{D_0t/\pi}\exp\left[\frac{-x^2}{4D_0t}\right]-x\,\mathrm{erfc}\left[\frac{x}{2\sqrt{D_0t}}\right]\right\}, \quad (5)$$

where C^0 is the bulk concentration $C(x,t=0)$ before current is switched on, D_0 is the molecular diffusion coefficient, n the number of exchanged electrons during the reduction process, and F the Faraday constant. If we try to fit the experimental cathodic profiles with this equation, keeping the same experimental values for the concentration C^0 and the current density, we realize that the fitting parameter D_0 must be given a quite unrealistic value. This is illustrated in Fig. 4(c) where three successive fits of the experimental data have been computed with Eq. (5) for the same times: 85, 150, and 240 s, respectively, and with a diffusion coefficient D_0 equal to 2×10^{-4} cm^2 s^{-1}. The fact that the diffusion coefficient is more than one order of magnitude greater than the molecular diffusion of zinc sulfate in water is a clear evidence that these experimental conditions are far from a purely diffusion-limited-growth process.

The shape of these cathodic profiles reminds us of those observable in forced convection systems (Nernst diffusion layer) [25]. Nevertheless, in our case there is no stationary diffusion layer thickness δ_N because the convection is not forced but natural, due to gravity forces [10,15]. Our interferometric analysis confirms the particle tracer study that has been done previously to measure the strength and the dynamics of gravity driven convection in thin gap electrochemical cells [10,26]. To pursue this comparison, we have recorded the propagation through the cell (towards the opposite electrode) of the foremost fringe on both cathodic and anodic sides. This corresponds exactly to the propagation of the convective roll that has been previously studied [10,26] and we confirm that the width $\delta(t)$ of the convective-diffusion layer scales as $\sqrt{t}$. Figure 5 shows a $\frac{1}{2}$ exponent scaling regime of $\delta(t)$ beyond approximately 40 s. This figure brings also the evidence of the preliminary regime (with a power law exponent close to $\frac{4}{5}$) that has also been reported in [10,26–28] and attributed to the intermediate settling of the convective roll. The $\frac{1}{2}$ exponent rather reflects the viscous diffusion of the roll front across the cell.

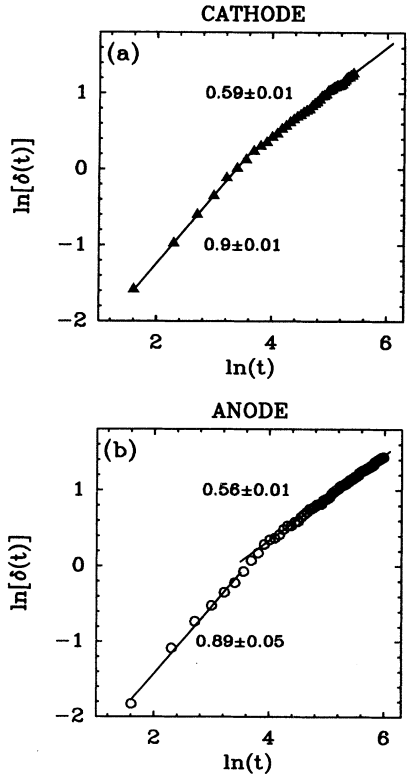

FIG. 5. Time evolution of the convective-diffusion layer thickness. The slopes are obtained by linear regression fit of the data (a) cathode, (b) anode. The parameter values are [$ZnSO_4$] = 1 mol l^{-1}, $j=150$ mA cm^{-2}, $W=5$ cm, $L=5$ cm, and $D=250$ μm.

If we look back at Fig. 4(c), we notice that the pure diffusion solutions of Eq. (5) match pretty well the evolution of the concentration profiles inside a bounded region (<1 mm) close to the cathode. This is the "linear" or quasilinear regime where x remains smaller than $\sqrt{D_0 t}$ and where Eq. (5) can be approximated by

$$C(x,t)=C^0-\frac{2j}{nF}\sqrt{t/\pi D_0}+\frac{jx}{nFD_0}\ . \tag{6}$$

The slope at the origin is therefore j/nFD_0, where D_0 is the phenomenological diffusion coefficient that has been already used to perform the whole concentration profile fitting. By computing the asymptotic slopes of the concentration profiles close to the cathode, we recover, as could be logically expected, the same diffusion coefficient as before: $D_0\simeq 2.10^{-4}$ cm^2 s^{-1}.

This straightforward calculation reveals a fundamental result in the context of growth processes, because it demonstrates that even in a complex system where convection, migration, and diffusion processes are simultaneously involved, the concentration gradients in a region of finite width close to the flat cathode remain linearly related to the current density:

$$\frac{\Delta C}{\Delta x}\sim\frac{j}{nFD_0}\ , \tag{7}$$

which is nothing else than the first Fick rule. The message of this interferometric analysis is that at a 1 mm length scale, the system can be considered as a pure diffusion one with an enhanced diffusion coefficient. This is a fundamental point as far as theoretical modeling of interfacial instability in electrodeposition is concerned. The crucial difference which remains, comparing electrodeposition with crystallization processes, is the dependence of the diffusion coefficient on both concentration and current density parameters, as well as the geometrical characteristics of the cell (gap and width). We can finally strengthen this good agreement between the local "diffusion-limited" approximation and our experimental data by plotting the evolution of the extrapolated concentrations at both anode and cathode interfaces versus the square root of time. Both evolutions are plotted in the same representation in Fig. 6, for the same parameter values as in Figs. 3–5. We observe that the concentration at the cathode fits perfectly the prediction of Eq. (6) and that one can also, from the measurement of the Sand's time where the interfacial concentration approaches zero, $t_S\sim 270$ s, recover again the value of the

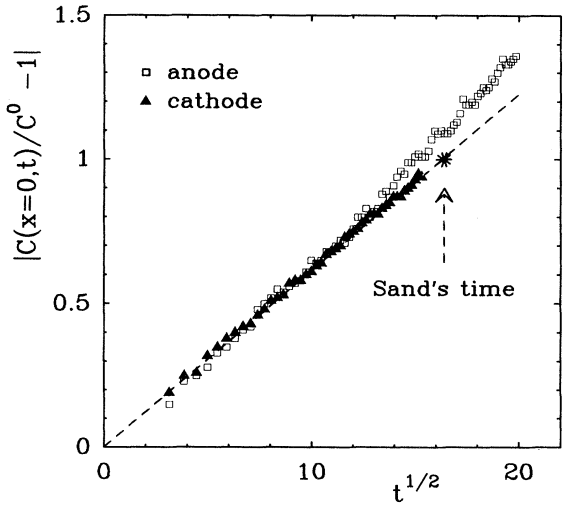

FIG. 6. Time evolution of the extrapolated concentration $C(x=0,t)/C^0$ from interferometric analysis of both anodic and cathodic parts of the electrodeposition cell. The filled triangles correspond to the cathode and the empty squares correspond to the anode. The parameter values are $[ZnSO_4] = 1$ mol l^{-1}, $j=150$ mA cm^{-2}, $W=5$ cm, $L=5$ cm, and $D=250$ μm.

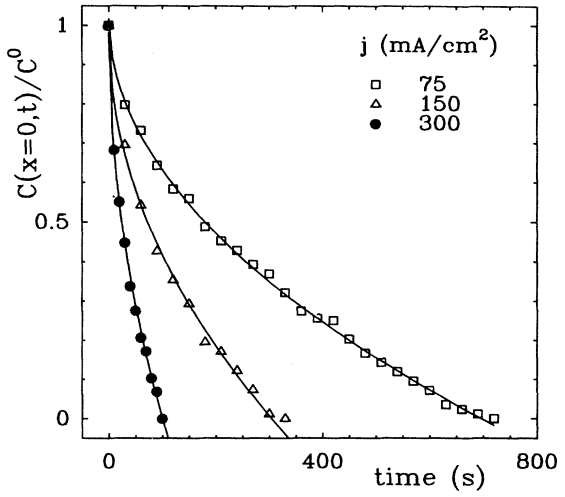

FIG. 7. Time evolution of the rescaled concentration $[ZnSO_4]_{x=0}/[ZnSO_4]_0$ versus time for different current density (respectively, $j=75$ mA cm^{-2}, $j=150$ mA cm^{-2}, and $j=300$ mA cm^{-2}). The plain curves are fits of the experimental data by the square root prediction of Sand's model. The parameter values are $[ZnSO_4] = 1$ mol l^{-1}, $W=8$ cm, $L=5$ cm, and $D=250$ μm.

diffusion coefficient D_0 by

$$\frac{j\sqrt{t_S}}{C^0} = \frac{nF\sqrt{D_0\pi}}{2}, \tag{8}$$

we find $D_0 \simeq 2\times10^{-4}$ cm^2 s^{-1}. Figure 6 also illustrates the concentration effect that has already been discussed above. When the system approaches the Sand's time, the concentration at the anode gets progressively higher than what could be predicted by a diffusion equation with a constant diffusion coefficient. This means that at the anode, the local convective diffusion process is smoothly evolving during the experiment because the concentration of zinc sulfate keeps increasing. From a macroscopic point of view, we observe the decrease of convective-diffusion coefficient D_0 and a bounding of the zone of greater zinc sulfate concentration close to the anode.

In Fig. 7, we have performed the same analysis for three different current densities at the cathode and plot the time evolution of the extrapolated concentration $C(x=0,t)$. We check that the product $j\sqrt{t_S}$ is not constant as could be expected in pure diffusion systems but that it increases with j. Let us mention that the measurement of t_S and D_0 by this method is subject to many sources of errors and with the statistics of five runs for each current value we could only afford a 15% uncertainty on t_S. The precise determination of the $D_0(j)$ curve requires, therefore, greater statistics than we have yet performed. This investigation is currently under progress.

To conclude this macroscopic study, we can emphasize again the powerfulness of this interferometric method to decode the relationship between the transport processes and the growth dynamics. In particular, in this preliminary study, we have shown that the first stage of the growth, prior to the complete depletion of the interface, can be locally considered as a diffusion-limited process.

C. Voltage signal analysis

The evidence of a Sand's time where the concentration at the interface should reach zero is nevertheless disturbing and unphysical because it would mean that the impedance of the cell would diverge at this time. Let us look at the voltage signal which corresponds to the same experiment as before. This signal is shown in Fig. 8. If we focus on the first 300 s of this signal, it looks globally a smoothly increasing curve over a period of about 270 s and then decreases beyond that time. We will not discuss the small amplitude oscillations that can be recorded in the zinc sulfate system and which have been already ex-

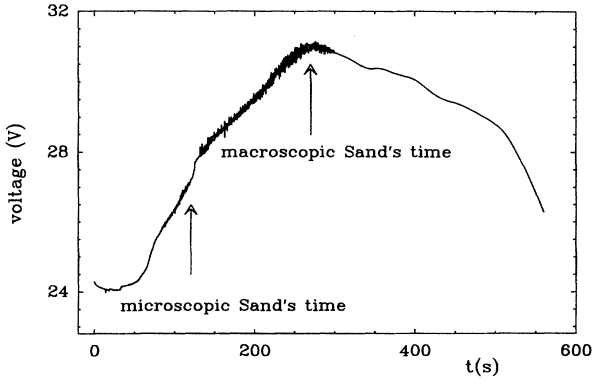

FIG. 8. Voltage signal (anode versus cathode voltage drop). The parameter values are $[ZnSO_4] = 1$ mol l^{-1}, $j=150$ mA cm^{-2}, $W=5$ cm, $L=5$ cm, and $D=250$ μm.

plained in terms of the competition between zinc and proton reduction in a preceding publication [9], but we can conclude from this observation that the depletion of the interface is already complete before the global voltage maximum. Oscillations start around 120 s because the system is forced to maintain a constant current even if the Zn^{2+} concentration is zero at the interface. Therefore an additional electrochemical process is started, i.e., the reduction of protons. At this time, the electrode becomes unstable but only on a microscopic scale. There must therefore be a first selection regime from 120 to 270 s, prior to the macroscopic Sand's time, which precedes the emergence of the well defined macroscopic whiskers that are shown in Figs. 3(d) and 3(e). The characteristic spatial wavelength of the large scale selection beyond 270 s is related to the size of the convective diffusion zone δ (the width of the zone of interference fringes).

If we look more precisely at Fig. 8 we observe two additional facts that need to be discussed. In the first 30 s, the voltage signal shows a preliminary decrease. This reflects the very fast polarization of the interface (double layer charging) which is rapidly damped by the triggering of the inner core of the buoyancy driven convection [10]. This phase corresponds to the $\frac{4}{5}$ exponent regime shown in Fig. 6. From 30 to 100 s, the voltage increases progressively, expressing the installation of the convective roll and the progressive depletion of the interface. Then at the real Sand's time (120 s), something occurs that our large scale analysis could not detect.

IV. MICROSCOPIC SCALE INTERFEROMETRIC ANALYSIS

Focusing our interferometer to smaller scales (a few 100 μm), we get the set of microscopic interferometric pictures of the neighborhood of the cathode which are shown in Fig. 9. At $t=10$ s, after current is switched on, a very small and bright fringe has settled close to the cathode. This bright fringe is the clue for the existence of very sharp concentration gradients close to the interface, much steeper than our preceding large scale analysis could predict. In Fig. 9(b), we have tried to plot the concentration profiles from the fringe patterns of Fig. 9(a). This is certainly not an accurate estimation of the concentration, given the shortness of the scale of estimation, because we are reaching the limitations of our experimental setup and light deflection also distorts the fringe pattern in this zone. Nevertheless, we think it worth showing that, in these electrochemical cells, we can clearly distinguish two zones where the concentration gradients are definitely distinct. This difference is obvious in the middle picture of Fig. 9(a) ($t=185$ s) and its corresponding concentration profile in Fig. 9(b).

Moreover, the fact that this sharp fringe could be observed even when the reference laser beam which does not cross the electrochemical cell is cut, as shown in the rightmost picture of Fig. 9(a), also confirms that in this zone of about 100 μm, the concentration gradient along the x direction is so steep that it can induce a strong bending of the beam in the direction of the positive gradient. This deviated part of the beam can therefore interfere with the part of the beam that has not deviated in the weaker concentration gradient zone ahead. Such effects have already been described in thicker cells in the past. We refer the reader to the abundant literature published in the 1970s on this subject [18–20].

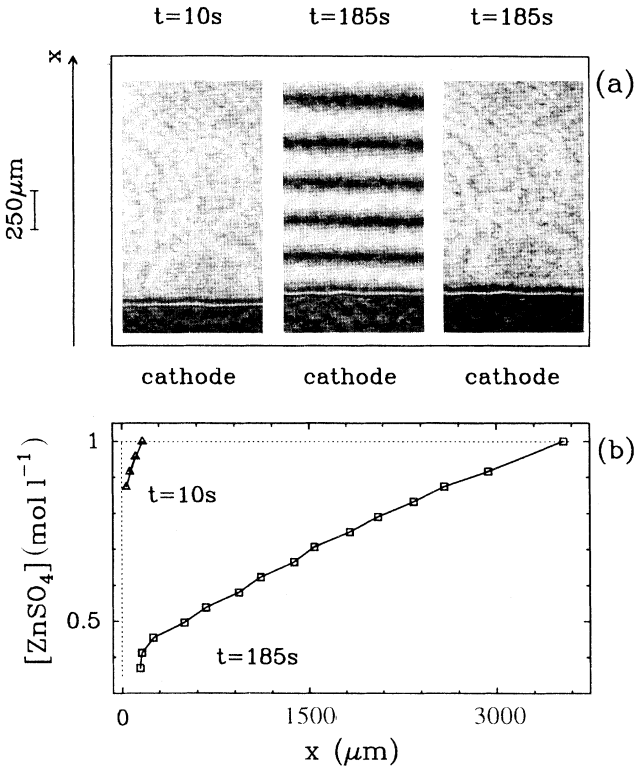

FIG. 9. Microscopic interferometric analysis of the first stage of zinc electrodeposition experiment. (a) The two leftmost pictures are interferometric pictures (two laser beams) for two successive times $t=10$ s and $t=185$ s. The rightmost picture has been obtained at $t=185$ s, keeping only the laser beam which crosses the electrochemical cell. (b) Concentration profiles computed from the interferometric patterns. The parameter values are $[ZnSO_4] = 1$ mol l^{-1}, $j=150$ mA cm^{-2}, $W=5$ cm, $L=5$ cm, and $D=250$ μm.

As far as the large scale fringes are concerned, we have checked afterwards that within the gap of 250 μm, the measured concentration gradients ($\sim 210^{-3}$ mol cm^{-4}) at large scale are not steep enough to produce a noticeable bending of the laser beam and a distortion of these fringes. Let us mention that such an effect has not been observed at the anode, since in that side, the laser beam is expected to be deflected towards the anode (increasing concentration zone).

Can we now relate the appearance of this bright and sharp fringe to some physical phenomena? The most immediate answer follows the discussion that we just developed earlier on density driven convection effects. To explain the rapid emergence of this small fringe, we need to revisit a question that has been approached in preceding papers [9,10]. In the very first seconds of the electrodeposition experiment, there is a very quick depletion of the zinc cations at a few atomic lengths of the metal interface itself, because these are going to be rapidly ad-

sorbed on it. This creates a narrow zone along the cathode, whose width is of the order of the depth of the cell (250 μm), where the transportation of ions, perpendicular to the electrode, is not convective but simply due to diffusion and migration. The slowness of the transport processes (with respect to convection) in this zone explains the sharpness of the concentration gradients. This zone of sharp gradient is bounded by the core of the convective roll and does not spread across the cell as can be noticed in Fig. 9(a). The comparison of the specific size of the small fringe ($\sim$100 μm) with the width ($\sim$125 μm) of the core of the convective zone supports our interpretation.

Moreover, the differentiation of the transport dynamics into two separate zones: a central core, whose size is invariant in time and a tail of this core which spreads across the cell by viscosity, is a good approximation of what really occurs in the cell, since it also provides a reasonable interpretation of the inflection zone of the voltage signal around 130 s (Fig. 8). Indeed, during the very first stage of the growth, inside the convective roll core, the depletion of the interface is faster than in its tail and there exists therefore a "microscopic" Sand's time which is actually the real time where the interfacial concentration of zinc sulfate reaches arbitrarily small values and where the electrode destabilizes a first time. The small size of this stiff depletion layer must produce much shorter wavelength selection than what has been observed beyond 300 s. It is exactly what occurs around 100 s; the growth proceeds through a first destabilization of its initial flat interface and smaller deformations occur. The second interfacial instability, around 260 s, must occur when these deformations reach the size of the inner roll core. The distinction between the first (120 s) and the second (270 s) instabilities is illustrated by plotting successive contours of the metal deposit, separated by a fixed interval ($\Delta T = 30$ s) in Fig. 10(a). The velocity difference of these two growth regimes is also presented in Fig. 11(a) where we have plotted the maximum velocity of the foremost tip of the interface versus time. We recover the two first transitions around 120 and 270 s that we have discussed and we also observe a third stage with a much higher velocity [Fig. 10(b) and Fig. 11(b)] that we will discuss in the next section.

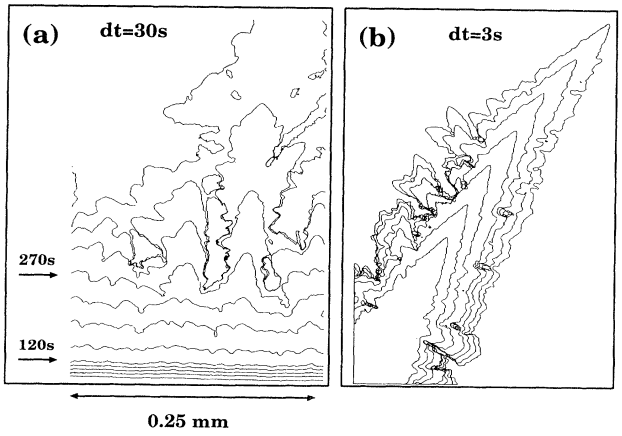

FIG. 10. Two-dimensional projection of the zinc electrodeposit contours obtained from successive pictures of the growth. (a) Selection of contours during the depletion regime; the two transitions are reflected by a modification of the velocity of the interface (marked by arrows). The time interval between each contour is $\Delta t = 30$ s. (b) Selection of contours after the second destablization of the interface ($t > 300$ s) $\Delta t = 3$ s. The parameter values are [$ZnSO_4$] = 1 mol l^{-1}, $j = 150$ mA cm^{-2}, $W = 5$ cm, $L = 5$ cm, and $D = 250$ μm.

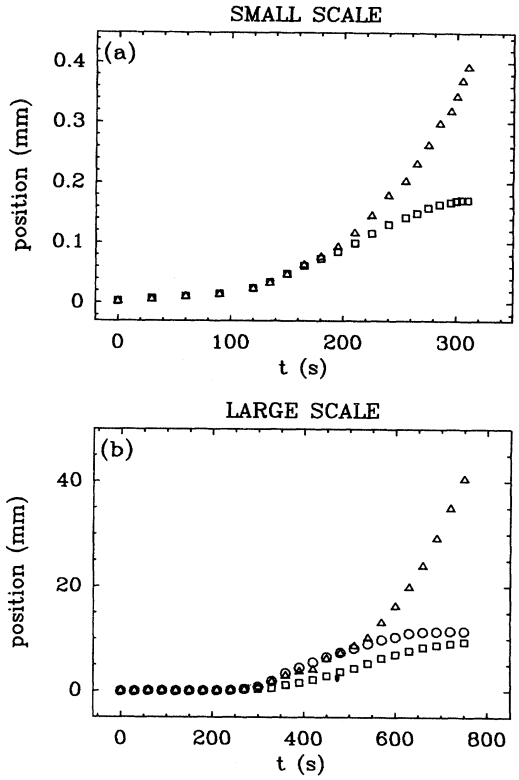

FIG. 11. Time evolution of the velocity of the different dendrites during the electrodeposition of zinc sulfate. (a) Microscale analysis of the velocity. (b) Macroscale analysis of the velocity. The empty triangles correspond to the foremost dendrites whereas the squares and circles correspond to dendrites that will be completely screened in the late stage of the growth. The parameter values are [$ZnSO_4$] = 1 mol l^{-1}, $j = 150$ mA cm^{-2}, $W = 5$ cm, $L = 5$ cm, and $D = 250$ μm.

The strong concentration gradient zone observed in Fig. 9 close to the cathode brings also a straightforward visualization of the location of the zones of electroactivity on the interface. In Fig. 12, the brighter fringes at the tips of the foremost dendrites lighten the zones of greater velocity.

It is important to mention that the interferometric pictures of the concentration map that we have presented are actually computed from averaged measurements of the index of the solution across the section of the cell, and that they do not give any information about the concentration map in a cross section of the cell. Such information can be obtained by confining a narrow channel of

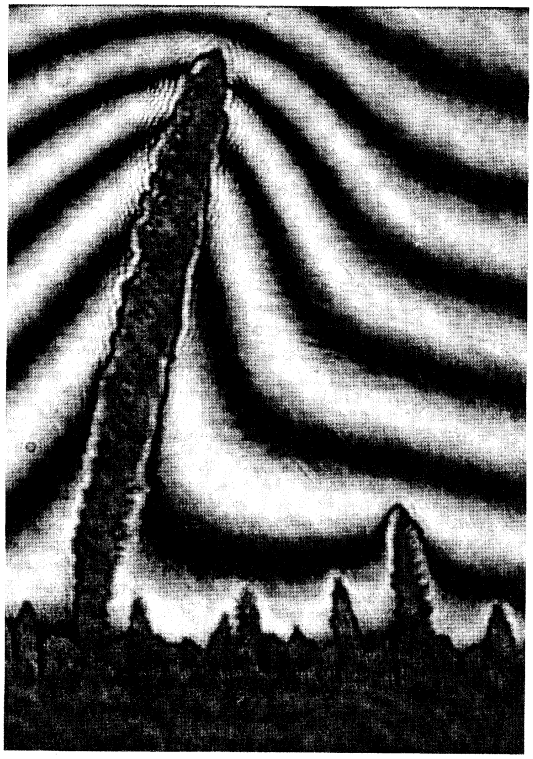

FIG. 12. Microscale interferometric picture of the second destabilization regime (just after the Sand's time) inside the convective roll. The parameter values are $[ZnSO_4] = 1$ mol l^{-1}, $j = 150$ mA cm^{-2}.

electrolyte between two Teflon wires (which delimit the lower and upper sides of the channel). These wires are themselves tightly clamped between two glass plates which define the side walls of the channel. The cell configuration is sketched in Fig. 13. The electrochemical cell has simply been moved in the interferometric table, to work with a horizontal laser beam, since the glass plates must now be vertical. Figure 14(a) shows the shape of isoconcentration contours, 30 s after the beginning of the experiment. Let us mention that the aspect ratio of this cell is very different from the one used in horizontal configuration (the channel is much narrower) and makes impossible a direct comparison of the time scales for the different transitions.

On Fig. 14(a), we notice that the fringes are not vertical, and that moreover these fringes give a striking evidence for the buoyancy-driven convective instability. At the cathodic side of the cell, the depletion of zinc sulfate by electroreduction makes the fluid lighter and unstable with respect to buoyancy forces [10,26–28]. An ascendant motion of the fluid is triggered close to the interface which drains the lighter fluid in the upper part of the cell. This motion is sketched by arrows in Fig. 14(a). This is what we have called the core of the convective roll. It manifests itself in Fig. 14(a) by the stacking of small fringes which are quite horizontal close to the cathode.

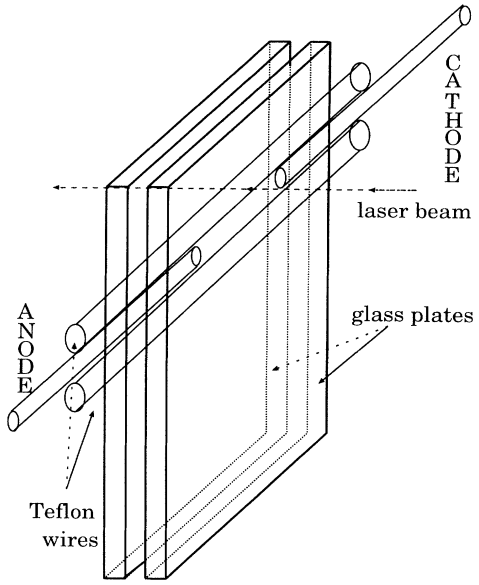

FIG. 13. Sketch of the vertical reactor that has been constructed for the cross sectional interferometric study.

We also notice in this picture that these fringes are bent when they invade the cell, like tongues of lighter fluid that would propagate across the cell along the upper side of the cell. This reflects exactly the large scale dynamics of the convective roll that has been evidenced in Ref. [10]. Further in the experiment [Fig. 14(b)], after the microscopic Sand's time, the first destabilization has already occurred and the growth remains bounded in the zone where the fringes are quasihorizontal. This picture gives a direct visualization of our preceding discussions.

V. THE LATE STAGE SELECTION REGIME

To complete our dynamical analysis we need now to look further in the time evolution and focus on the very late stage of the growth process. Let us have one more look at the voltage signal beyond 300 s (Fig. 8). After the

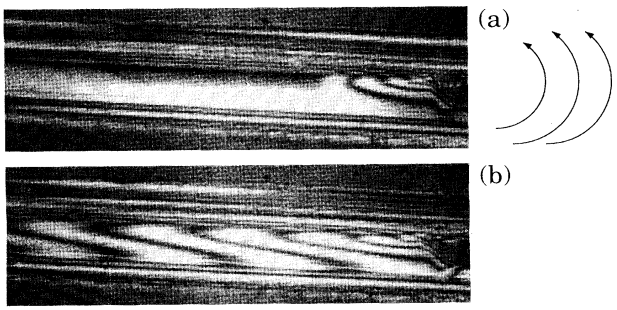

FIG. 14. Microscopic interferometric analysis in a cross section the electrodeposition cell. A microcapillary cell with a rectangular section (250 μm$\times$250 μm) has been constructed by confining two calibrated Teflon wires (distant of 250 μm) between two glass plates and fitting two 250 μm zinc wires at each end. (a) $t = 30$ s, (b) $t = 400$ s. The parameter values are $[ZnSO_4] = 1$ mol l^{-1}, $j = 150$ mA cm^{-2}.

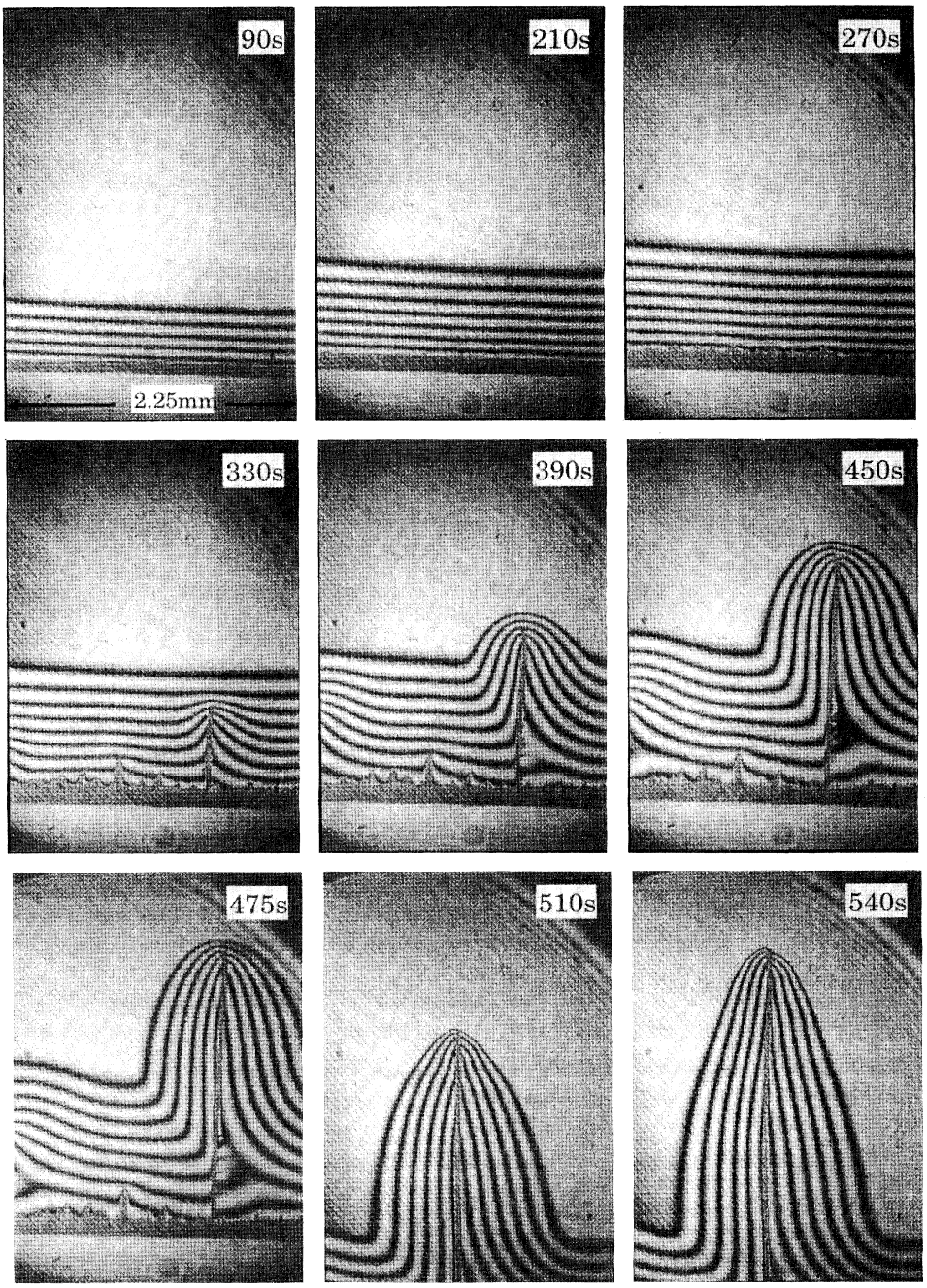

FIG. 15. The history of the zinc electrodeposition through the Mach-Zehnder interferometer optics: beyond 380 s one single dendrite is breaking the convective diffusion layer and stops all its neighbors. The parameter values are $[ZnSO_4] = 1$ mol l^{-1}, $j = 150$ mA cm^{-2}, $W = 5$ cm, $L = 5$ cm, and $D = 250$ μm.

voltage extrema that we have correlated to the macroscopic instability of the interface, we distinguish two phases of different slopes. The first one corresponds to a rather slow decrease of the voltage and to the selection process between the different dendrites which just emerged from the cathode, inside the convective-diffusion region. The second one corresponds to a much faster growth regime where the electric screening between branches is much stronger. There, only a few dendrites (one or two) remain active and capture the whole current on their tip. The analysis of the time evolution of the maximum velocity of the interface [Fig. 11(b)] brings an additional evidence of the modification of the dynamics that occurs after the breaking of the convective diffusive roll by the leading dendrite. Beyond 500 s, the velocity of the foremost dendrite of the deposit increases abruptly. After the dendrite has crossed the convective roll (zone of parallel fringes in Fig. 15), its frontal concentration gradient gets much steeper in space and shrinks to the size of the inner convective roll. This speeds up immediately its velocity. Simultaneously, the local current density is strongly amplified at its tip, which amplifies even more its speed. There is a highly nonlinear feedback process which leads to a rapid selection of very few dendrites in-

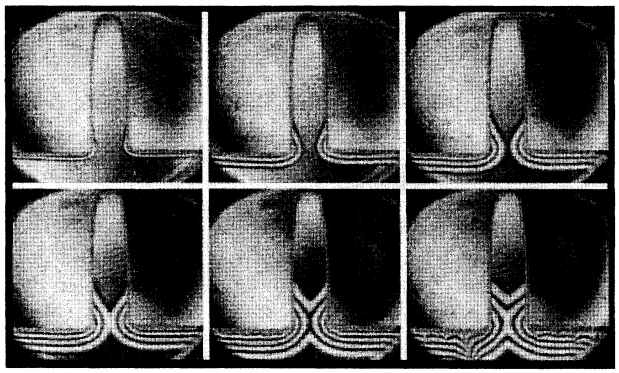

FIG. 16. Interferometric visualization of the influence of the shape of the cathode on the local thickness of the deposit. These pictures have been taken at successive times of zinc electrodeposition, and show that the depletion of the interface does not occur inside the U, below its width. We visualize with interferometry an empirical rule that has been used for years by electroplaters.

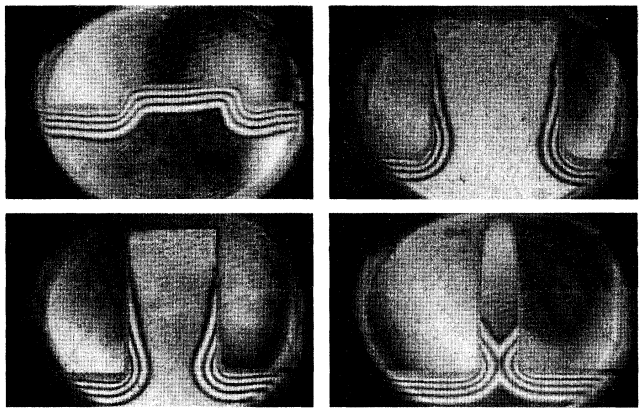

FIG. 17. Interferometric visualization of the influence of the aspect ratio of a U-shaped cathode on the local electroactivity of thermal interface. These four pictures have been taken at the same time, beyond the Sand's time and we observe that for an aspect ratio of depth/width greater than 1, there is no zinc deposited on the bottom of the U-shaped cathode, confirming the dynamical prediction of the preceding figure.

side the cell.

Let us also notice in Fig. 15 the asymmetry of the fringes on both sides of the emerging whisker at 390 s. On the right side of its backbone, at $\frac{1}{3}$ of its height, the interferometry reveals a local modification of the concentration of zinc sulfate. This fringe distortion is likely to be the clue to a dissolution effect that we have already observed in preceding experiments with the sudden alteration of the already grown part of the deposit in the back side of the growing tip. The voltage drop across the whisker stem can be sufficient for a single whisker to play both the role of cathode and anode locally. This is also amplifying the velocity of the whisker. Let us note that such a deposition-dissolution process requires a fast interfacial charge transfer kinetics, that is, small overpotentials for both reduction and oxidation processes of the metal. The fact that one single sharp whisker captures on its tip the majority of the current density creates a very strong electric field around the tip.

This screening effect can be very important for electroplating problems. To conclude this paper, we want therefore to emphasize also the relevance of such interferometric studies for the optimization of electroplating techniques for complex geometric objects. If we take a U-shaped cathode, the two-dimensional representation of a hole (which causes serious problems for electroplaters), that we confine, as usual, between two glass plates, we get an immediate visualization of the active area for a given geometry (Fig. 16). Changing the ratio between the depth and the width of the hole, we recover the empirical rule used for electroplating that beyond the minimum aspect ratio of 1, the bottom is no longer electroactive because of the screening and therefore no coating occurs (Fig. 17). The shape of the fringes for such a geometry can be useful for investigating the actual influence of inorganic additives that are used to smooth the zinc deposits and to minimize their inhomogeneities. We hope to elaborate on this point in a future communication.

ACKNOWLEDGMENTS

We thank B. Pouligny, F. Texier of the Centre de Recherche Paul Pascal for fruitful discussions. This work was supported by the Centre National d'Etudes Spatiales under Grant No. 92/097 and the Direction des Recherches et Etudes Techniques under Grant No. 93/0409. The work of A.K. was also supported by the Pinguin Foundation.

[1] *On Growth and Form, Fractal and Non-fractal Patterns in Physics,* edited by H. E. Stanely and N. Ostrowski (Martinus Nijhog, Dordrecht, 1986).

[2] T. Vicsek, *Fractal Growth Phenomena* (World Scientific, Singapore, 1992).

[3] *The Physics of Structure Formation,* edited by W. Güttinger and G. Dangelmayr (Springer, Berlin, 1987).

[4] J. M. Garcia-Ruiz, E. Louis, P. Meakin, and L. M. Sander, *Growth Patterns in Physical Sciences and Biology* (Plenum, New York, 1993).

[5] J. R. Melrose, Chemometrics Intelligent Lab. Syst. **15**, 231 (1993).

[6] J. N. Chazalviel, Phys. Rev. A **42**, 7355 (1990).

[7] V. Fleury, J. N. Chazalviel, and M. Rosso, Phys. Rev. Lett. **68**, 2492 (1992); Phys. Rev. E **48**, 1279 (1993).

[8] A. Kuhn and F. Argoul, J. Electroanal. Chem. **371**, 93 (1994); Phys. Rev. E **49**, 4298 (1994); Fractals **1**, 451 (1993).

[9] F. Argoul and A. Kuhn, J. Electroanal. Chem. **359**, 81 (1993); Physica A **213**, 209 (1995).
[10] J. M. Huth, H. L. Swinney, W. D. McCormick, A. Kuhn, and F. Argoul, Phys. Rev. E **51**, 3444 (1995).
[11] A. Kuhn, Ph.D. thesis, Université de Bordeaux, France, 1994.
[12] P. P. Trigueros, F. Sagues, and J. Claret, Phys. Rev. E **49**, 4328 (1994).
[13] R. H. Cork, D. C. Pritchard, and W. Y. Tam, Phys. Rev. A **44**, 6940 (1991).
[14] D. Barkey, J. Electrochem. Soc. **138**, 2912 (1991).
[15] D. P. Barkey, D. Watt, Z. Liu, and S. Raber, J. Electrochem. Soc. **141**, 1206 (1994).
[16] F. R. McLarnon, R. H. Muller, and C. W. Tobias, Electrochimica Acta, **21**, 101 (1976).
[17] Y. Fukunaka, T. Yamamoto, and Y. Kondo, J. Electrochem. Soc. **136**, 3630 (1989).
[18] R. H. Muller, in *Advances in Electrochemistry and Electrochemical Engineering,* edited by P. Delahay and C. W. Tobias (Wiley Interscience, New York, 1972), Vol. 9, p. 281.
[19] F. R. McLarnon, R. H. Muller, and C. W. Tobias, J. Electrochem. Soc. **129**, 2210 (1982).
[20] F. R. McLarnon, Ph.D. thesis, University of California, 1974.
[21] R. N. O'Brien, W. F. Yakykyshyn, and J. Leja, J. Electrochem. Soc. **110**, 820 (1963).
[22] Y. Fukunaka, T. Minegishi, N. Nishioka, and Y. Kondo, J. Electrochem. Soc. **128**, 1274 (1981).
[23] W. H. Steel, *Interferometry* (Cambridge University Press, Cambridge, England, 1983).
[24] R. J. Goldstein, in *Measurements of Heat Transfer,* edited by E. R. G. Eckert and R. J. Goldstein (Springer-Verlag, Berlin, 1976), p. 241.
[25] A. J. Bard and L. R. Faulkner, *Electrochemical Methods, Fundamentals and Applications* (Wiley, New York, 1980).
[26] J. M. Huth, Ph.D. thesis, University of Texas at Austin, 1995.
[27] V. Fleury, J. H. Kaufman, and D. B. Hibbert, Phys. Rev. E **48**, 3831 (1993); Nature (London) **367**, 435 (1994).
[28] M. Rosso, J. N. Chazalviel, V. Fleury, and E. Chassaing, Electrochem. Acta **39**, 507 (1994).

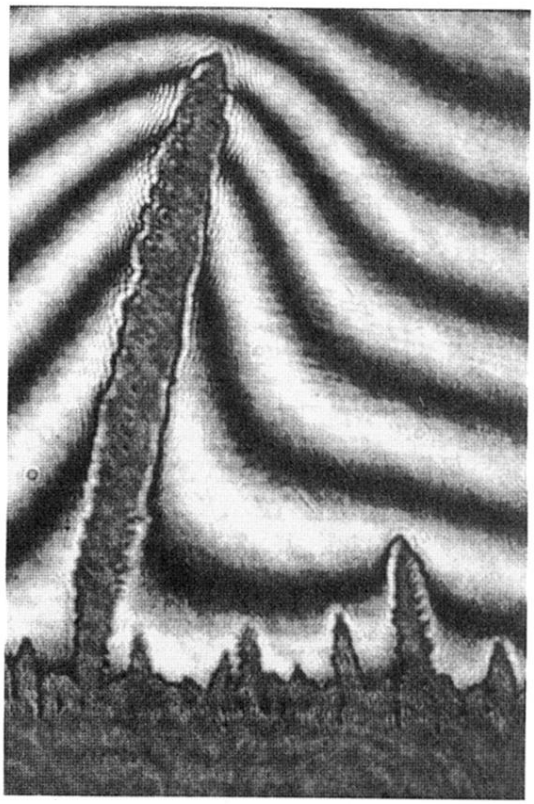

FIG. 12. Microscale interferometric picture of the second destabilization regime (just after the Sand's time) inside the convective roll. The parameter values are $[ZnSO_4] = 1$ mol l^{-1}, $j = 150$ mA cm^{-2}.

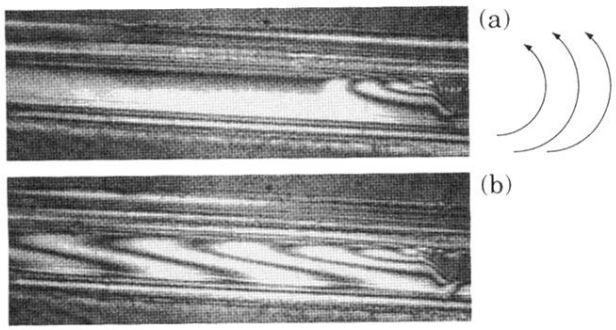

FIG. 14. Microscopic interferometric analysis in a cross section the electrodeposition cell. A microcapillary cell with a rectangular section (250 μm$\times$250 μm) has been constructed by confining two calibrated Teflon wires (distant of 250 μm) between two glass plates and fitting two 250 μm zinc wires at each end. (a) $t=30$ s, (b) $t=400$ s. The parameter values are $[ZnSO_4] = 1$ mol l^{-1}, $j=150$ mA cm^{-2}.

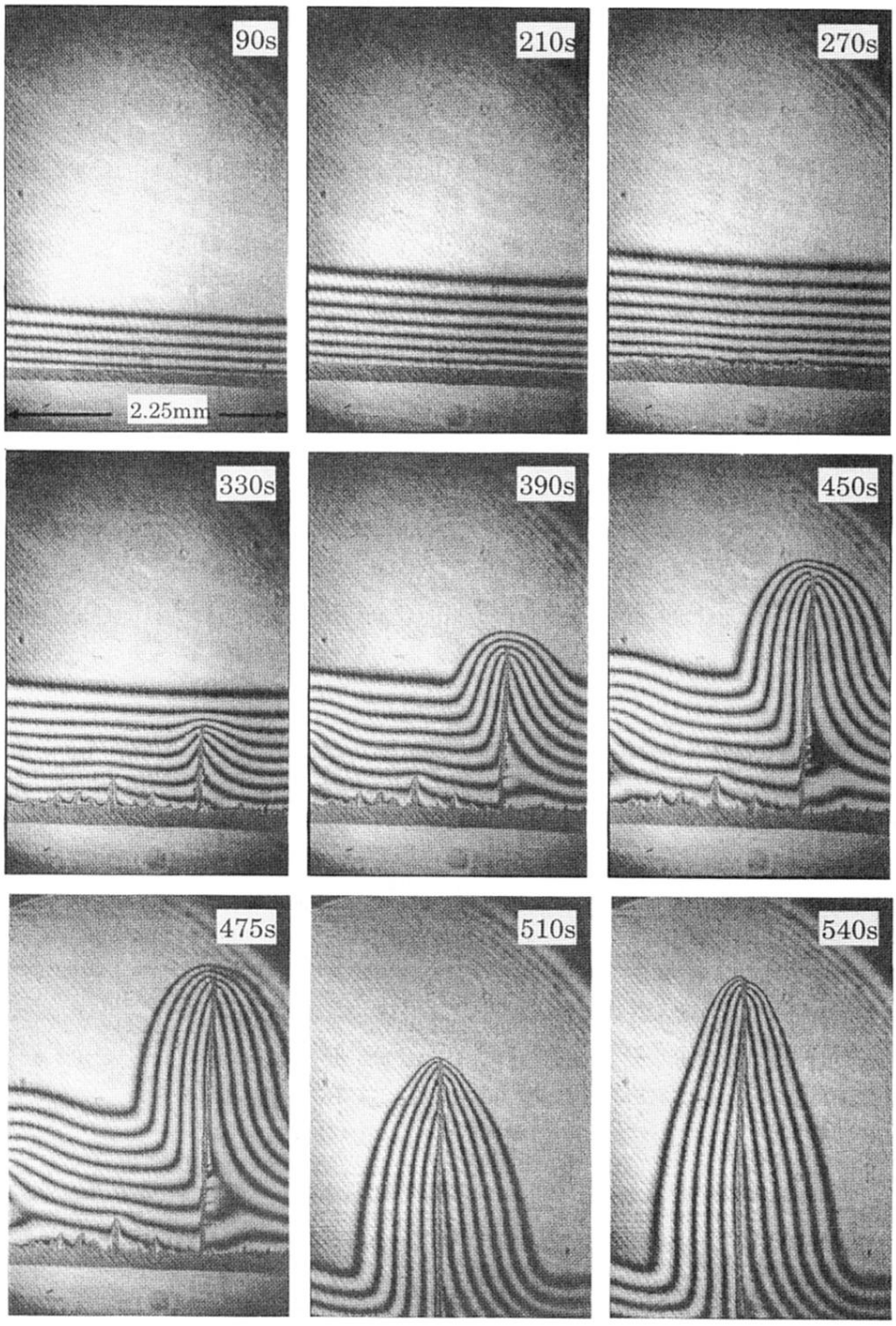

FIG. 15. The history of the zinc electrodeposition through the Mach-Zehnder interferometer optics: beyond 380 s one single dendrite is breaking the convective diffusion layer and stops all its neighbors. The parameter values are $[ZnSO_4] = 1$ mol l^{-1}, $j = 150$ mA cm^{-2}, $W = 5$ cm, $L = 5$ cm, and $D = 250$ μm.

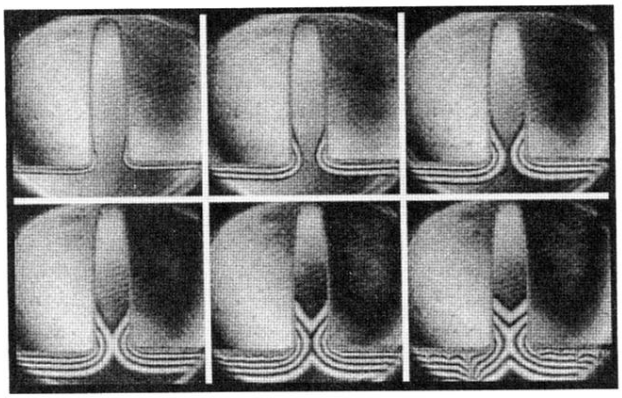

FIG. 16. Interferometric visualization of the influence of the shape of the cathode on the local thickness of the deposit. These pictures have been taken at successive times of zinc electrodeposition, and show that the depletion of the interface does not occur inside the U, below its width. We visualize with interferometry an empirical rule that has been used for years by electroplaters.

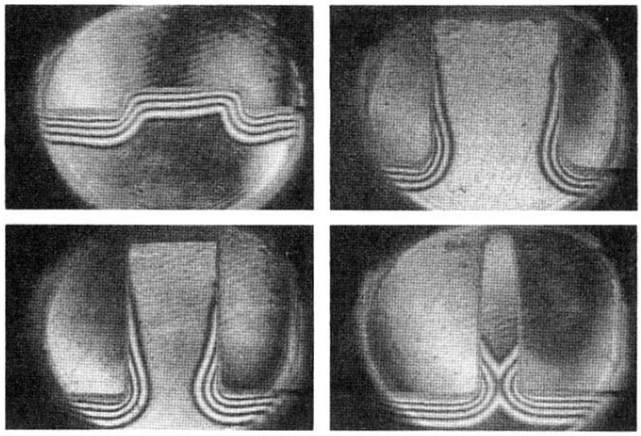

FIG. 17. Interferometric visualization of the influence of the aspect ratio of a U-shaped cathode on the local electroactivity of thermal interface. These four pictures have been taken at the same time, beyond the Sand's time and we observe that for an aspect ratio of depth/width greater than 1, there is no zinc deposited on the bottom of the U-shaped cathode, confirming the dynamical prediction of the preceding figure.

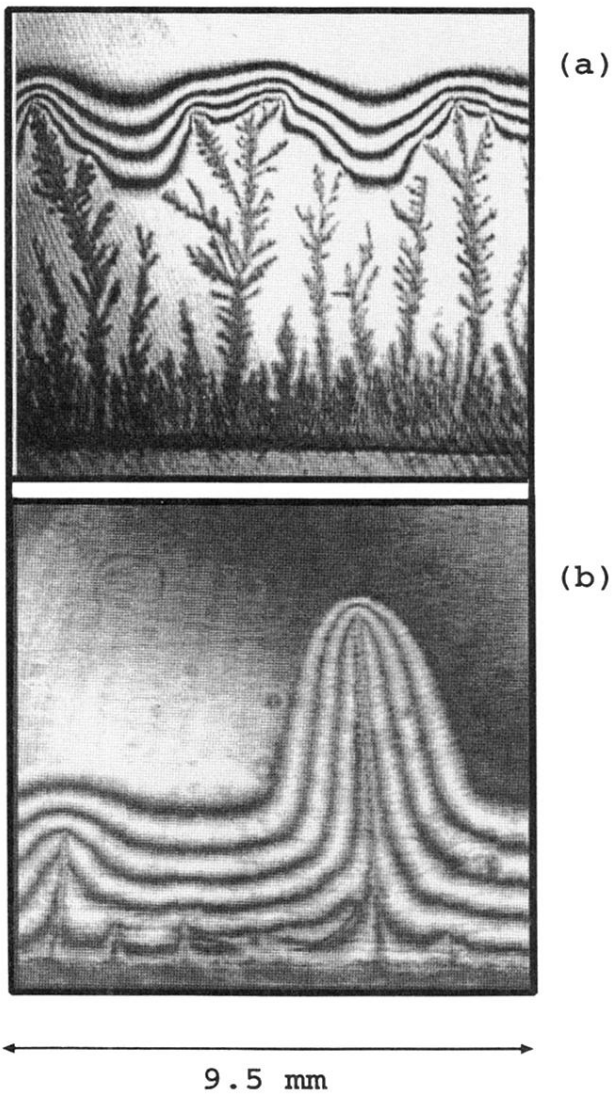

FIG. 2. Grey scale representation of interferometric imaging of the concentration field around zinc electrodeposits. The experimental parameters are, respectively, (a) $[ZnSO_4] = 1$ mol l^{-1}, $j = 50$ mA cm^{-2}, (b) $[ZnSO_4] = 0.5$ mol l^{-1}, $j = 150$ mA cm^{-2}. The geometrical characteristics of the cell are width $W = 5$ cm, length $L = 5$ cm, depth $D = 125$ μm in (a) and $D = 250$ μm in (b).

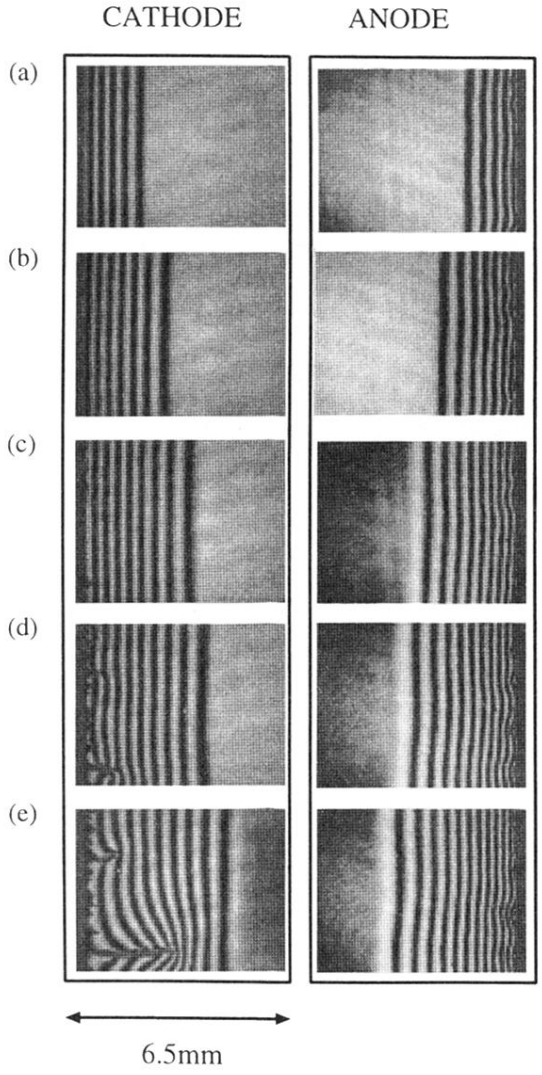

FIG. 3. Macroscopic interferometric images of thin gap electrodeposition of zinc at different times of the growth process. (a), (b), (c), (d), and (e) are digitized pictures given by the Mach-Zehnder at five successive times $t=85$ s, $t=150$ s, $t=240$ s, $t=300$ s, $t=440$ s, respectively. The parameter values are $[ZnSO_4] = 1$ mol l^{-1}, $j=150$ mA cm^{-2}, $W=5$ cm, $L=5$ cm, and $D=250$ μm.

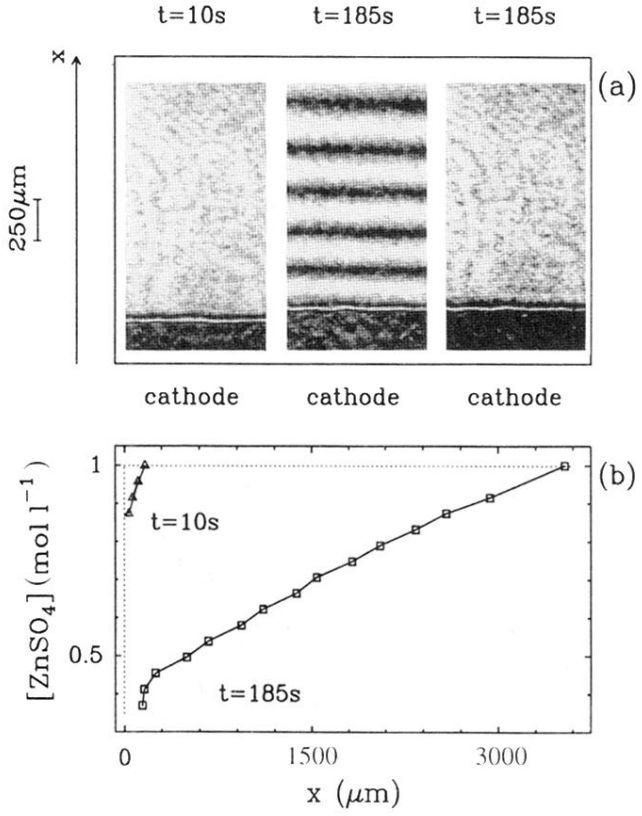

FIG. 9. Microscopic interferometric analysis of the first stage of zinc electrodeposition experiment. (a) The two leftmost pictures are interferometric pictures (two laser beams) for two successive times $t=10$ s and $t=185$ s. The rightmost picture has been obtained at $t=185$ s, keeping only the laser beam which crosses the electrochemical cell. (b) Concentration profiles computed from the interferometric patterns. The parameter values are $[ZnSO_4] = 1$ mol l^{-1}, $j=150$ mA cm^{-2}, $W=5$ cm, $L=5$ cm, and $D=250$ μm.